J. Fluid Mech. (1991), *vol.* 229, *pp.* 87–114
Printed in Great Britain

Experiments on periodically forced flow over topography in a rotating fluid

By JOHN M. PRATTE† AND J. E. HART
Department of Astrophysical, Planetary and Atmospheric Sciences, University of Colorado, Boulder, CO 80309, USA

(Received 6 July 1990 and in revised form 8 January 1991)

Results from laboratory experiments on oscillatory flows over topography in a rapidly rotating cylinder of homogeneous liquid are presented and compared with weakly nonlinear and low-order theories. With periodic forcing, the motion can be either periodic or chaotic. In the periodic regime, linear Rossby waves excited by the sloshing flow over shallow bottom topography become resonant at forcing frequencies that are integer multiples of the natural free Rossby wave frequency. As the topographic effect or the forcing amplitude is increased, the maximum response is shifted away from the linearly resonant frequency; to higher periods for azimuthal topographic wavenumbers of 1 and to lower periods for topographic zonal wavenumbers exceeding 1, in agreement with theory. The simple theories which use slippery sidewalls do not describe the observed chaotic flows. These complex states are associated with the development of small-scale vortices in the sidewall boundary layer that are shed into the interior. For both periodic and chaotic flows, long-time particle paths can contain significant chaotic components which are revealed in direct Poincaré sections constructed from observations of surface floats.

1. Introduction

The important geophysical problem of the nature of airflow over large-scale mountains has led to much previous work on the response of a rotating fluid when a steady zonal (eastward or westward) current is incident on a set of ridges or isolated bumps. For example, Charney & Devore (1979) and Hart (1979) showed that steadily forced flow over shallow hills could exhibit multiple stationary equilibria which were considered of potential significance for atmospheric blocking. Recent observations of coastal ocean currents driven by fluctuating surface wind stresses, for example by Denbo & Allen (1983), stimulated studies of the dynamics of periodically forced rotating systems with variable bottom topography. Haidvogel & Brink (1986) used a numerical model to show that periodic wind stresses could produce a mean alongshore current in a homogeneous quasi-geostrophic fluid moving over a sinusoidal bottom. Samelson & Allen (1987) and Allen, Samelson & Newberger (1991) studied the properties of periodically forced rapidly rotating flow over a set of long ridges using analytical methods. Again a retrograde mean current was predicted. In addition, a chaotic flow response was found for certain parameter settings.

The present paper reports results from laboratory experiments on periodically forced quasi-geostrophic flow over topography in a rapidly rotating cylinder. Our

† Current address: Shell Offshore Inc., PO Box 61933, New Orleans, LA 70160, USA.

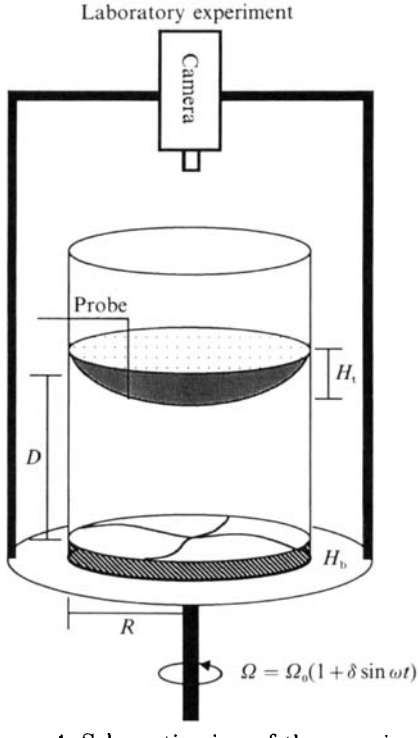

FIGURE 1. Schematic view of the experiment.

goals are to explore the utility of weakly nonlinear and low-order models in a geometrically simple and controlled setting, to study the transition between periodic and chaotic regimes while relating the latter to specific flow structures, and to investigate the nature of parcel trajectories, which may be chaotic even when the flow itself is periodic. The laboratory experiments provide data on expected flow regimes, and indicate that the viscous sidewall boundary layer, which is neglected in the theories, plays an important role in the observed Eulerian chaos.

Figure 1 displays a schematic view of the apparatus used in the experiments. A polyvinylchloride cylinder of radius $R = 22.54$ cm contains a homogeneous water layer of mean depth $D = 10.0$ cm. The upper water surface is free and the bottom consists of a specific fixed topography. Two topographic functions were used. The simplest, both geometrically and from a fabrication point of view, is the uniform slope (hereafter denoted US)

$$H_b^* = h_b \frac{r^*}{R} \cos(\theta), \tag{1}$$

where r^* is the radius and θ is the polar angle measured from the crest in the direction of the basic rotation $\boldsymbol{\Omega}$. The relative topographic amplitude h_b/D is easily adjusted by changing the slope, but note that this azimuthal wavenumber-1 function contains a wide spectrum of the basic radial modes of the linear theory which are simply Bessel functions of index 1 with zeros at $r^*/R = 1.0$.

An alternative wavenumber-2 form, hereafter denoted FB, is

$$H_b^* = h_b J_2\left(\frac{\alpha_{21} r^*}{R}\right) \cos(2\theta), \tag{2}$$

where J_2 is the Bessel function of the first kind with index 2. The eigenvalue $\alpha_{21} = 5.41$ is chosen so that J_2 is zero at $r^* = R$ ($r = 1$). This single-wave Fourier–Bessel topography has the advantage that it is an eigenfunction of the linear theory. The construction of this surface is described in detail by Pratte (1990). Basically it is rough cast using DOW D.E.R. 331 resin then hand polished within 3% of the desired shape. However, because the procedure was so time consuming, only one unit was made, with $h_b = 2.08$ cm. Equation (2) describes one possible component of a general Fourier–Bessel decomposition of arbitrary topography which vanishes at the sidewall.

Motion is driven by modulating the basic rotation rate $\boldsymbol{\Omega}$ according to

$$\boldsymbol{\Omega} = \boldsymbol{\Omega}_0(1 + \delta \sin(\omega t)). \tag{3}$$

The rotation vector is parallel to the axis of the cylinder. The modulation $\delta \ll 1$ so that the motions have small flow Rossby number. That is, if $2\delta\Omega_0 R$ is used as the relative velocity scale U, then the Rossby number $R_0 \equiv U/2\Omega_0 R$ is equal to δ. The physical manifestation of (3) is obtained by using a geared-down stepper motor to control the rotation rate of the turntable upon which the cylinder is placed. The stepper motor is driven from a voltage-controlled oscillator with an output pulse rate that is a function of a given sinusoidal input voltage. This latter signal is derived from a precision low-frequency oscillator. The output amplitude is then linearly related to δ and the frequency is proportional to ω. The stability of the driving system is about 0.001 of Ω_0 with the errors being greater in δ than in ω.

Under rotation the free surface becomes deformed into a parabola given, in a time average, by

$$H_t^* = \frac{\Omega_0^2 r^{*2}}{2g}, \tag{4}$$

where g is the gravitational acceleration. This upper parabolic surface acts as a zonally (i.e. azimuthally) invariant form of topography which can be shown to be equivalent to the β-effect of meterology and oceanography (cf. Hart 1972; Pedlosky 1987). With respect to the oceanographic problems mentioned above, the upper surface may be thought of as generating an alongshore-invariant deepening of the ocean layer as one moves towards $r^* = R$. In the quasi-geostrophic limit a fluid which shallows towards R is dynamically similar to one which deepens towards R, but with east and west reversed.

We consider that the external Froude number

$$H_T = \frac{\Omega_0^2 R^2}{2gD} \tag{5}$$

is small enough so that dynamical effects at the interface are negligible. The appropriate measure of vortex stretching via *dynamic* free-surface deformations compared to the time-rate-of-change of relative vorticity is H_T/α_{nm}^2, where α_{nm} is the mode number of the Rossby wave excited by the topography. Because $\alpha_{mn}^2 > 13$ for all our experiments, and H_T is typically about 0.2, the assumption that the interface is dynamically fixed is justified. However, the topographic β-effect arising from the large static parabola (4) is very important because it forces a stretching of fluid columns that move radially.

Table 1 lists the relevant dimensional and non-dimensional parameters for the experiments. There are five independent non-dimensional parameter groups which

	Dimensional parameters
$D = 10.0$ cm	mean layer depth
$R = 22.54$ cm	radius of cylinder
$\rho = 1.00$ g/cm^3	fluid density (water)
$\nu = 0.01$ cm^2/s	kinematic viscosity
$g = 980$ cm^2/s	gravitational acceleration
$\Omega_0 = 2.85$ rad/s	mean rotation rate (unless otherwise stated)
ω (rad/s)	forcing frequency
τ (s)	forcing period
	Coordinates
r	non-dimensional radius, scaled by R
θ	polar angle in direction of rotation
u	radial velocity, scaled by $R\omega$
v	azimuthal velocity, scaled by $R\omega$
t	time, scaled by ω^{-1}
	Non-dimensional parameters
n	azimuthal wavenumber of the topography
α_{nm}	mth radial eigenvalue of the topography
$\delta = (\Omega_{\max} - \Omega_0)/\Omega_0$	forcing amplitude or flow Rossby number
$\epsilon = \omega/2\Omega_0$	frequency Rossby number
$E = \nu/2\Omega_0 D^2 = 1.75 \times 10^{-5}$	vertical Ekman number
$E_L = \nu/2\Omega_0 R^2 = 3.4 \times 10^{-6}$	lateral Ekman number
$H_T = \Omega_0^2 R^2/2gD = 0.21$	external Froude number (upper surface height)
$H_B = h_b/D$	bottom surface height
$Q = E^{\frac{1}{2}}/\sqrt{2\epsilon}$	bottom friction
$\beta = nH_T/\epsilon\alpha_{nm}^2$	planetary vorticity gradient (β-effect)
$\beta\eta = n\delta/2\epsilon$	vorticity advection
$S = n\delta H_B/2\epsilon^2\alpha_{nm}^2$	topographic forcing

TABLE 1. Basic parameters and scaling for the experiments and the model

appear explicitly in the equation of motion, (8), and an investigation of a large volume of parameter space is therefore impractical. In this study we have chosen to fix several of the variables at geophysically relevant sizes and vary those which are most easily manipulated; the modulation frequency and amplitude, and to a lesser extent the topography. Thus, E, E_L, and H_T are fixed while the other parameters Q, β, $\beta\eta$, and S vary as ϵ and δ are changed. Details on the measurement techniques will be given as the data are presented. The rest of the paper is organized as follows. Section 2 contains a brief review of the weakly nonlinear and low-order theories. Section 3 discusses the periodic flow response, while §4 describes the transition between periodic and chaotic flows. Section 5 provides data on parcel trajectories as visualized by tracking surface floats. The conclusions are found in §6.

2. Review of the theory

In this section we briefly summarize the formulation and predictions of two models for the motion in the cylinder. Both start from the one-layer quasi-geostrophic vorticity equation written in coordinates attached to the cylinder and rotating with the modulated rotation rate $\boldsymbol{\Omega}$. Because the Rossby numbers (i.e. δ and ϵ) are small, the motion is horizontal and two-dimensional to lowest order. Although the coordinates are modulating, the modulation just leads to sinusoidal source of vertical vorticity, uniform in space. This can be balanced, for small friction, by a simple solid-

body sloshing motion. The total velocity relative to coordinates attached to the modulating cylinder is then given non-dimensionally by

$$v = -\frac{\delta r}{2\epsilon}\sin(t) + \frac{\partial \Psi}{\partial r}, \tag{6}$$

$$u = -\frac{1}{r}\frac{\partial \Psi}{\partial \theta}, \tag{7}$$

for the azimuthal and radial components, respectively. The stream function $\Psi(r, \theta, t)$ is proportional to the geostrophic pressure and represents disturbances to the basic sloshing motion. The geostrophic balance expressed in (6) and (7) represents a balance between pressure gradients and mean Coriolis forces associated with the dominant time-averaged component of the basic rotation $\boldsymbol{\Omega}$.

The basic oscillatory solid rotation represented by the first term on the right-hand side of (6) is obtained from the full vorticity equation in coordinates attached to the cylinder in the limit as Q becomes small (Hart 1990). In the experiments reported in this paper, $Q = (\nu\Omega_0)^{\frac{1}{2}}/D\omega$ is typically of order or less than 0.1, a value obtained, for example, with $D = 10$ cm, $\Omega_0 = 2.85$ rad per s, $\nu = 0.01$ cm^2 s^{-1}, and a forcing period of 40 s. The basic state including the effects of Ekman bottom friction will be phase shifted in time by an amount of order Q, with an amplitude $1/(1+Q^2) \approx 1$ times that shown in (6).

The deviation from the solid-body sloshing motion is governed by the quasi-geostrophic vorticity equation

$$\frac{\partial \nabla^2 \Psi}{\partial t} + \mathrm{J}\left[\Psi - \frac{\delta r^2 \sin(t)}{2\epsilon}, \nabla^2 \Psi + \frac{H_\mathrm{B} f(r,\theta) - H_\mathrm{T} r^2}{\epsilon}\right] = -Q\nabla^2 \Psi + \frac{E_\mathrm{L}}{\epsilon}\nabla^4 \Psi. \tag{8}$$

This is obtained by expansion in the small parameter δ. The Jacobian advection operator

$$\mathrm{J}(A, B) \equiv \frac{1}{r}\left(\frac{\partial A}{\partial r}\frac{\partial B}{\partial \theta} - \frac{\partial A}{\partial \theta}\frac{\partial B}{\partial r}\right),$$

and $f(r, \theta)$ is the non-dimensional topography structure function (e.g. $r\cos(\theta)$). The basic physical effects are advection of potential vorticity (relative vorticity plus fluid column depth) by the sloshing motion, advection by the resulting flow disturbance itself, Ekman bottom friction (the first term on the right), and lateral diffusion of relative vorticity (the last term on the right).

A more detailed derivation of (8) is given in Hart (1990) who presents a weakly nonlinear, hereafter denoted WNL, theory based on this equation. The WNL model neglects sidewall friction and replaces the real no-slip outer wall boundary condition with that of no normal flow only. This simplification is typical of all the models discussed in the introduction. By comparing theory with experiments, Hart (1972) showed that such a theory does a good job at describing weakly nonlinear two-layer motions associated with baroclinic instability provided that E_L is small. Whether or not viscous sidewall effects are important at finite amplitude is a subject that is addressed here experimentally. Numerical modelling of the full equation (8), with lateral friction and a rigid wall at $r = 1$, is quite difficult for the parameter settings of interest, and experiments provide useful data on the behaviour of the real fluid system.

Hart (1990) considers one spectral topographic component at a time. The linear motion is normally of amplitude $O(S)$, which is presumed small. However, the linear theory becomes resonant (with amplitudes of order SQ^{-1}, which may be large) at all $\beta = j$, where j is an integer. This linear resonance occurs when the frequency of forcing is equal to an integer multiple of the natural frequency of a Rossby wave with the spatial structure of the bottom topography (i.e. a given wavenumber n and radial eigenvalue α_{nm}). In order to determine what happens when nonlinearity and dissipation compete with forcing in near-resonant conditions, the WNL theory expands the stream function Ψ as

$$\Psi = \sigma\Psi_1 + \sigma^2\Psi_2 + \sigma^3\Psi_3 + \ldots, \tag{9}$$

where $\sigma \equiv S^{\frac{1}{3}} \ll 1$. The solution for the resonant mode is

$$\Psi_1 = \mathrm{Re}\,(A(t')\,\mathrm{e}^{\mathrm{i}\chi(t)}J_n(\alpha_{nm}\,r)), \tag{10}$$

with $\chi \equiv \beta t + \beta\eta\cos(t) + n\theta$. A weakly nonlinear cascade then finds the slow-time (t') amplitude equations for A by expansion and removal of secularities. In this model it is assumed that $\beta = j + \Delta$, $\Delta \approx \sigma^2$, and $Q \approx \sigma^2$. It is found that the correction field Ψ_2 consists solely of a time-independent retrograde zonal flow component.

The conclusions from the WNL model relevant to the present laboratory study are

(i) The solutions of the three ordinary differential equations describing the slow-time behaviour always fall onto a fixed point, leaving a fast-time spatially wavy oscillation of constant amplitude along with a second-order retrograde mean zonal flow proportional to $S^{\frac{2}{3}}\Psi_{2r}(r)$.

(ii) The resonance curve, which for the linear model is centred on $\beta = j$, is bent by nonlinear effects. The peak Ψ response is shifted off of $\beta = j$ by an amount $\Delta_{\max} = \Delta_{\max}(S, \eta, Q, j, b_n)$, where b_n is a wave-mean interaction integral tabulated in WNL. The qualitatively significant finding is that single-humped topographies of wavenumber $n = 1$ (like (1)) have a super-resonant peak response ($\Delta > 0$, or period τ higher than that required for linear resonance), while topographies with wavenumbers higher than 1 (like (2)) have a subresonant peak response ($\Delta < 0$, or period τ lower than that required for linear resonance).

(iii) There is a small region of parameter space where multiple steady solutions for $A(t')$ can exist for the same external parameters. These were shown to occur on a parameter plane with coordinates

$$\xi^{-3} \equiv \frac{S^2 b_n |I_j|^2}{(\beta - 1)^3}, \quad \frac{\mu^2}{\xi^2} \equiv \frac{Q^2}{(\beta - j)^2}. \tag{11}$$

Three solutions, two of which are stable, are found inside a nearly triangularly shaped region with vertices at $[(0,0), (-4/27, 0), (-8/27, 1/3)]$. Outside this 'triangle', one solution is predicted. (In Hart 1990 the terms in (35) and (36) involving $(3\mu^2/\delta^2 - 1)$ were misprinted, and should be raised to the 3 and 1.5 powers in the respective equations.)

Although the WNL model successfully demonstrates that the origin of the mean zonal current is through the action of bottom form drag in association with the asymmetry of Rossby wave propagation, it substantially overestimates its magnitude for all but the most small of S-values. This feature causes the WNL model to fail in its description of the laboratory experiments for most of the parameter domain studied here. We have found that a low-order model (denoted LO), which includes the interaction of the induced zonal current with the topography, gives a

superior description of the experimental results. In summary, the sloshing induced by the modulation of the basic rotation of the tank generates a Rossby wave motion when going over the seamounts. These waves rectify to generate a correction to the sloshing. This zonal flow correction (which includes a retrograde mean component) itself flows over the topography to produce a correction to the wave field. This latter effect is scaled out of the weak interactions in the WNL model (consistently so for small $S^{\frac{1}{2}}$).

The derivation of the alternative LO model is straightforward. The topography is assumed to consist of a single Fourier–Bessel eigenfunction $J_n(\alpha_{nm} r)$. The stream function Ψ is written as

$$\Psi = [X(t)\cos(n\theta) + Y(t)\sin(n\theta)]\, J_n(\alpha_{nm} r) + Z(t)\,\Phi(r), \tag{12}$$

where

$$\Phi(r) \equiv \int_0^r \frac{J_n^2(\alpha_{nm} r')}{r'}\,\mathrm{d}r' \tag{13}$$

is the self-consistent zonal jet forced by the single-wave self-interactions. Like the solutions of the WNL model, this wave and zonal current have no flow through the wall at $r = 1$, but the azimuthally wavy field does not satisfy no-slip there. Equation (12) is substituted into (8), with E_{L} set to zero, and the nonlinear terms are projected onto the three fundamental spatial modes that have amplitudes X, Y, and Z. Non-zero projections outside this limited set (which do exist) are truncated. This procedure yields three first-order nonlinear differential equations:

$$\frac{\mathrm{d}X}{\mathrm{d}t} = -QX + \beta(1+\eta\sin(t))\,Y - nC_1\,YZ, \tag{14}$$

$$\frac{\mathrm{d}Y}{\mathrm{d}t} = -QY - \beta(1+\eta\sin(t))\,X + nC_1\,XZ + S\sin(t) - \frac{nH_{\mathrm{B}}\,C_2}{\epsilon\alpha_{nm}^2}\,Z, \tag{15}$$

$$\frac{\mathrm{d}Z}{\mathrm{d}t} = -QZ + \frac{nH_{\mathrm{B}}}{2\epsilon}\,Y. \tag{16}$$

The interaction integrals are

$$C_1 \equiv K_1 + \frac{K_2}{\alpha_{nm}^2}, \quad C_2 \equiv K_1 \tag{17}$$

with

$$K_1 = \frac{2}{J_n'^2(\alpha_{nm})}\int_0^1 \frac{1}{r} J_n^4(\alpha_{nm} r)\,\mathrm{d}r, \tag{18}$$

$$K_2 = \frac{2}{J_n'^2(\alpha_{nm})}\int_0^1 J_n^2(\alpha_{nm} r)\frac{\mathrm{d}}{\mathrm{d}r}\left(\frac{1}{r}\frac{\mathrm{d}}{\mathrm{d}r}J_n^2(\alpha_{nm} r)\right)\mathrm{d}r. \tag{19}$$

For the FB topography with $n = 2$ and $m = 1$, $K_1 = 0.536$ and $K_2 = -10.70$.

Equations (14)–(16) are identical in form to those studied by Samelson & Allen (1987, equations 2.11), if their zonal flow U is decomposed into an externally forced oscillatory part and a zonal flow correction. They considered anisotropic topography, where the low-order truncation becomes asymptotically accurate in the limit of long ridges oriented perpendicular to the zonal current. Because of this different geometry, the numerical values of the externally controlled coefficients in each term are not the same as obtained for our experimental conditions, but the fundamental dynamical processes represented are similar. The infinite ridge topography is

somewhat ungeophysical and difficult to produce in the laboratory. Even though our topography is not anisotropic, in applying this model to our problem we find that for a substantial range of parameters the neglect of higher wave–wave interactions has little effect, and that model is dramatically better than the WNL one. We shall, however, show examples where the single-wave truncation (12) does lead to a failure of the low-order model.

The linear model of Hart (1990) can be recovered from (14)–(16) by dropping all nonlinear terms as well the last term on the right of (15). The WNL model can be obtained by performing the slow-time expansion about the linear mode with $C_2 = 0$. Indeed the last term on the right of (15) represents precisely the effect of the nonlinearly induced zonal current in producing a correction to the wave field, whereas the last term in (16) represents the topographic form-drag effect responsible for the generation of the zonal flow correction itself.

The LO and WNL models give similar results as $S \to 0$. However, for 'moderate' S ($S^{\frac{1}{3}}$ about 0.1 or greater), the resonance curve bending and regions of multiple equilibria can be substantially different. For example, the multiple resonances which lead to substantial responses at most integer values of β in WNL are not always found in LO, especially at small δ where only the lowest $\beta = 1$ resonance peak rises above the background in LO. Further differences in the models will become apparent as they are compared with the laboratory data.

3. The periodic flow regime

The flow $\boldsymbol{v}(\boldsymbol{r}, t)$, distinct from the Lagrangian particle paths obtained by integrating $\mathrm{d}\boldsymbol{r}/\mathrm{d}t = \boldsymbol{v}$, can either be periodic or chaotic. We first discuss the periodic regime because it is directly comparable with the theories of §2 that exhibit periodic solutions. That is, the WNL slow-time equations evolve to stable fixed points, leaving a periodic motion given by (10) with A constant. Numerical LO model solutions appear to become periodic after initial transients decay away for all parameters even remotely accessible experimentally. The parameter limits of the experimental periodic regimes and the domains of Eulerian chaos will be given in §4.

Experimental data on the flow were obtained by using a hot-thermistor anemometer located at a fixed point just below the upper free surface. Heat carried away from the probe by the motions causes a resistance change proportional to the local fluid velocity. Because the thermistor bead is spherical, the response is omnidirectional and we assume that the signal corresponds primarily to the speed of the dominant two-dimensional flow as given by (6) and (7). Calibration was repeatedly achieved using step changes in turntable rotation with a flat bottom inserted in the tank. The thermistor is inserted from above and has a diameter of about 0.7 mm, producing negligible disturbance to the motion. For most of the following discussion the probe is at $r = 0.50$, and $\theta = 5.7$ rad (FB topography) or $\theta = 1.6$ rad (US topography). Although the detailed time traces are dependent on probe position, the qualitative state of the fluid globally is captured at this single location. Pratte (1990) describes additional data from other probe positions. The data are logged into a computer using a 16-bit digitizer. Each run was started either from a previous state or from rest, with a 10 to 20 min transient decay time before data were taken. It was observed that the asymptotic endstate of all experiments with topography was achieved very rapidly, in several forcing cycles. The tank was covered with a lid to minimize evaporation and wind stress effects.

Figure 2 shows typical experimental and theoretical time series for the speed at the

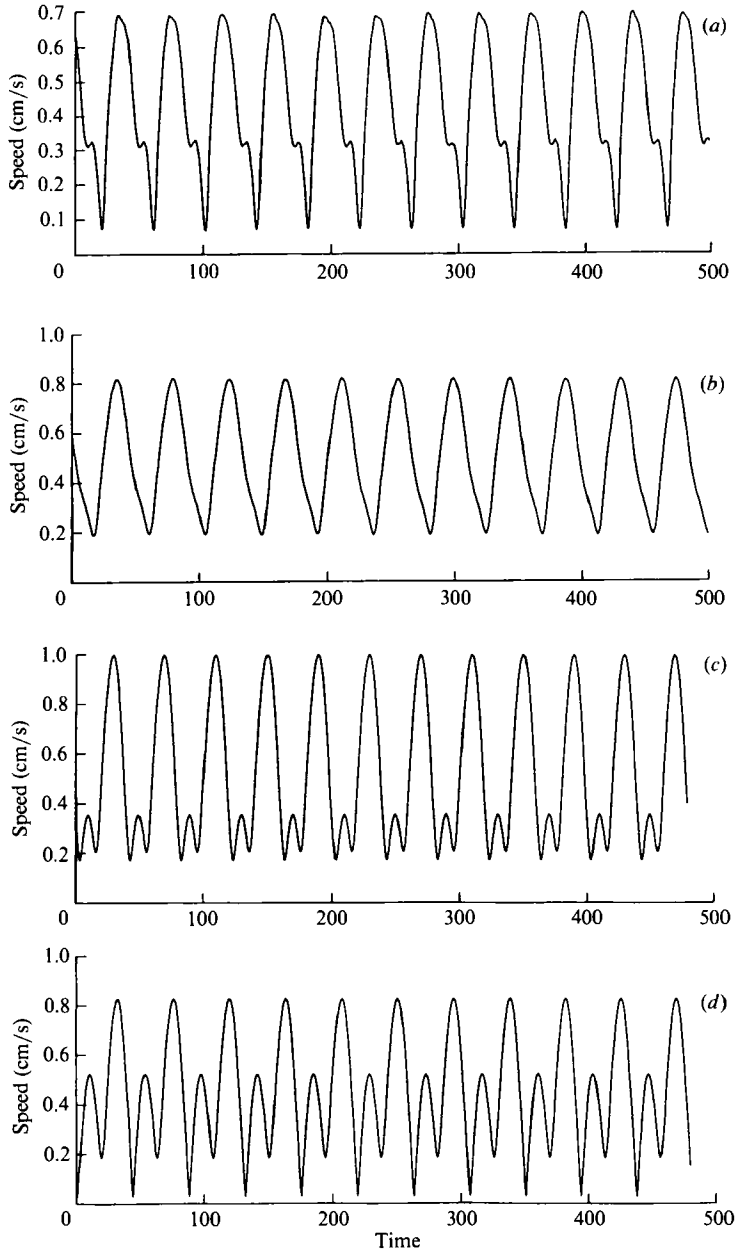

FIGURE 2. Time traces from the speed probe for US topography with $H_B = 0.05$ and $\delta = 0.02$. Experimental: (*a*) $\tau = 40.0$ s, (*b*) $\tau = 43.7$ s; WNL model: (*c*) $\tau = 40.0$ s, (*d*) $\tau = 43.7$ s.

probe with a small US topography. The signals contain harmonics which result from the advection of vorticity by the sinusoidal basic sloshing (the $\eta \sin(t)$ terms in (14) and (15), see also the solutions in Hart 1990 for the WNL model). The comparison between theory and experiment is not exact because the WNL model does not displace the resonance peak to as supercritical a value of the forcing period as is observed. However, the waveforms at the respective resonance peaks (figures 2*b* and 2*c*) have nearly equal amplitudes and means. The theoretical one shows more second harmonic in the troughs, but experiments and modelling show this aspect of the time

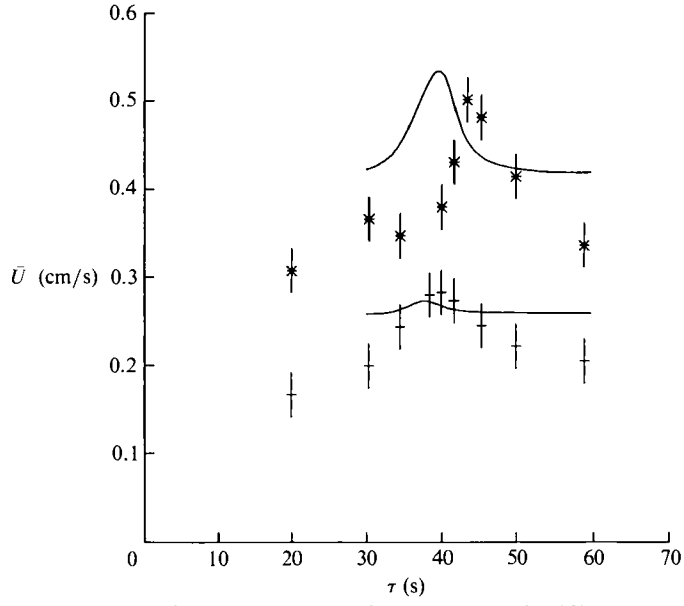

FIGURE 3. Average speed per cycle versus forcing period for US topography and *, $\delta = 0.01$, $H_B = 0.02$; +, $\delta = 0.02$, $H_B = 0.05$; ——, WNL model.

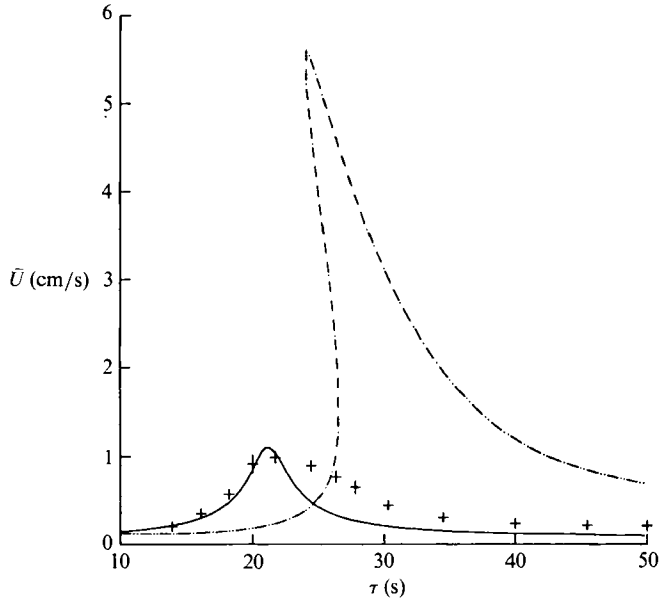

FIGURE 4. Average speed per cycle versus forcing period for FB topography with $\delta = 0.005$: +, experimental runs; ·–·–·–, WNL model; ——, LO model.

series is sensitive to precise probe location. Insofar as the theory does not have a viscous sidelayer at $r = 1$, the effective probe location for the experiment, which does, may be somewhat different. The overall response for flow over a shallow slope is summarized in figure 3. The linear resonance point is at $\tau = 37.5$ s. The WNL model is strictly valid near resonance as it is an expansion for $\beta = j + \Delta$, where Δ is assumed of order $S^{\frac{2}{3}} \ll 1$. At the linear resonance ($\tau = 37.5$), $S^{\frac{2}{3}} \approx 0.04$ for the $\delta = 0.02$

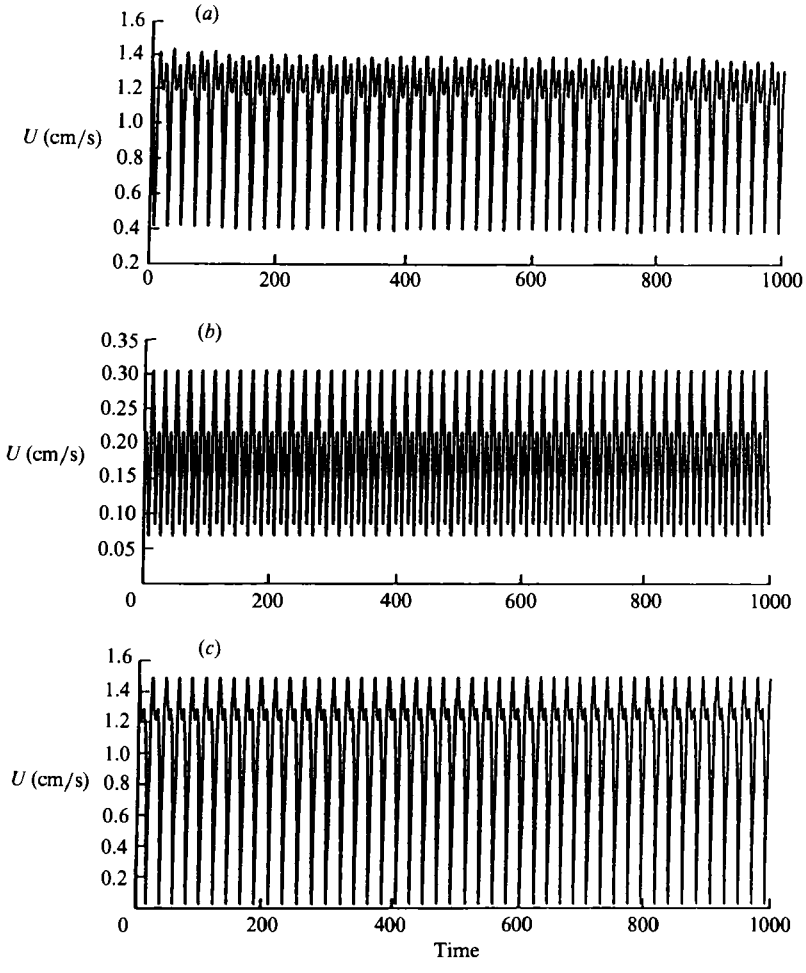

FIGURE 5. Time traces from the speed probe for FB topography with $\delta = 0.005$ and $\tau = 20.0$ s ($\epsilon = 0.55$) for (*a*) experiment, (*b*) WNL model, (*c*) LO model.

case. At near-resonant τ the curve amplitudes and shapes are similar, although the model underpredicts the resonance peak shift. Off the resonance, one should take account of the fact that the US topography forces motions at more than one radial mode. Because both the WNL and LO models are based on just a single wave they do not reproduce the tails of the curves very well.

Figure 4 shows a comparison with the single-wave FB topography at small δ. For this topography with wavenumber $n = 2$ the linear resonance at $\beta = 1$ occurs at $\tau = 34.7$ s. The peak response is now subresonant as forecast by both the WNL and LO models. The data fit the predictions of the LO model fairly well, especially at subresonant and near-resonant values of τ, but the WNL theory completely overestimates the resonant peak and predicts multiple equilibria that are not observed. Although the values of $S \approx 0.01$ are similar to those in figure 3, in the WNL model the amplitude of the zonal correction Ψ_2 at $\tau \approx 24$ s is ten times bigger than for the slope case because the other parameters (specifically μ and ξ) are different. This large value of Ψ_2 leads to a divergence in the series (9) in which the higher-order terms are larger than the leading term. Figure 5 displays typical time series comparisons for subresonant conditions. The LO model gives an accurate prediction

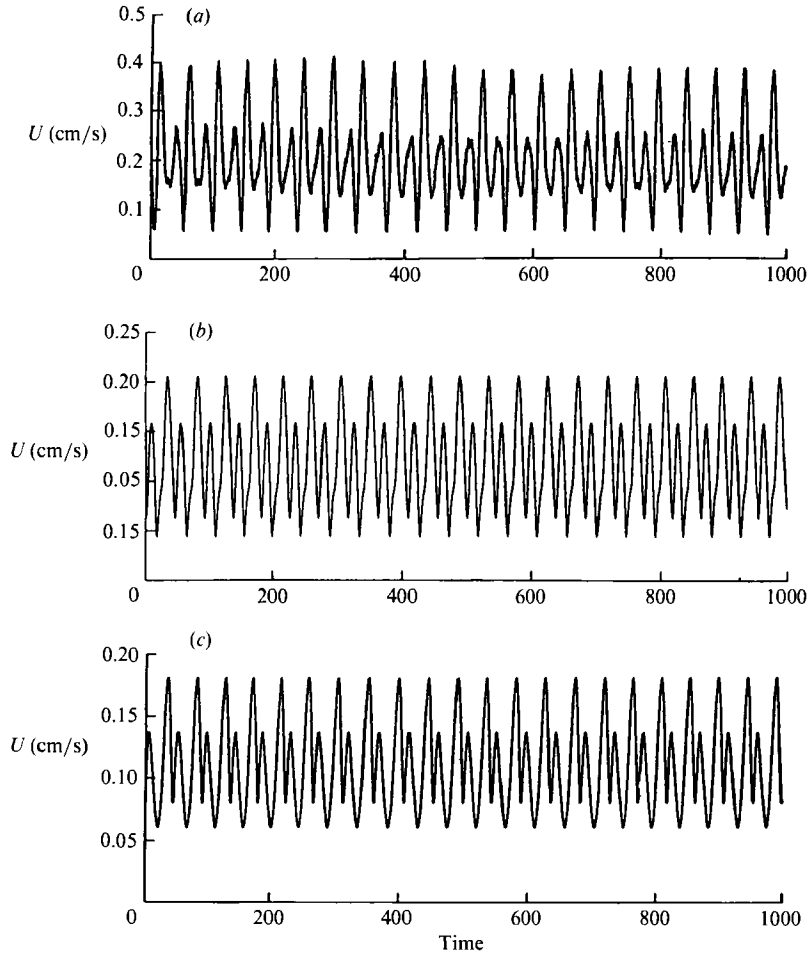

FIGURE 6. Time traces from the speed probe for FB topography with $\delta = 0.005$ and $\tau = 45.5$ s ($\epsilon = 0.024$) for (*a*) experiment, (*b*) WNL model, (*c*) LO model.

of the experimental results, while the WNL theory is very inaccurate. Figure 4 indicates that as τ is increased past the resonance peak the LO model begins to break down. Recall that the LO model is valid at all τ where the spatial truncation is realistic, but that the WNL theory applies only near resonance. Figure 6 shows comparisons of time series at $\tau = 45.5$ s, where both models are only fair. The $j = 1$ WNL prediction corresponding to the laboratory data in figure 6(*a*) is very poor, but the $\beta = j = 2$ WNL expansion (shown in figure 6*b*) does better since the second *nonlinear* resonance peak is close to $\tau = 50$ s.

At larger δ, where S becomes bigger, the disparity between the two models grows. Figure 7 shows that the WNL theory now grossly overpredicts the observed speeds because $S^{\frac{1}{3}} \approx 0.5$ and the zonal correction $\Psi_2(r, \beta, \eta, Q, S)$ is itself huge. The LO model does well near the $j = 1$ and $j = 2$ resonance peaks (the $j = 1$ linear resonance is still at $\tau = 34.7$ s), but is not very good in the valley between the two peaks, nor at τ greater than about 42 s. Figure 8 displays experimental and LO model time traces just to the left of the second peak. The comparison is not nearly as favourable as that near the main subcritical peak at 20.4 s where S is substantially smaller (not shown; the traces are similar to those in figures 5*a* and 5*c*).

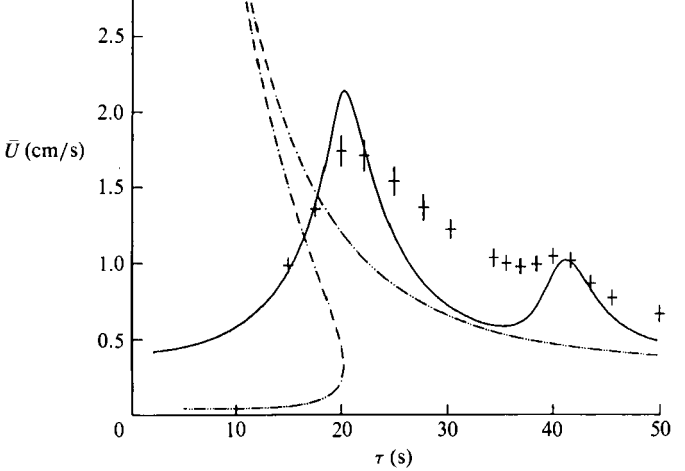

FIGURE 7. Average speed per cycle versus forcing period for FB topography with $\delta = 0.02$: +, experiment runs; ·–·–, WNL model; ——, LO model. WNL model curve is 0.1 actual size.

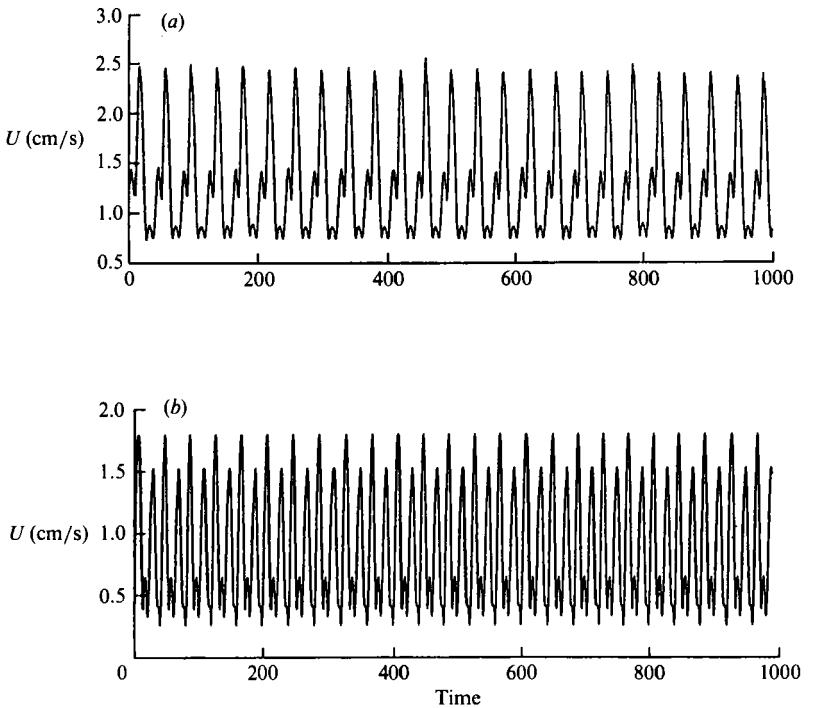

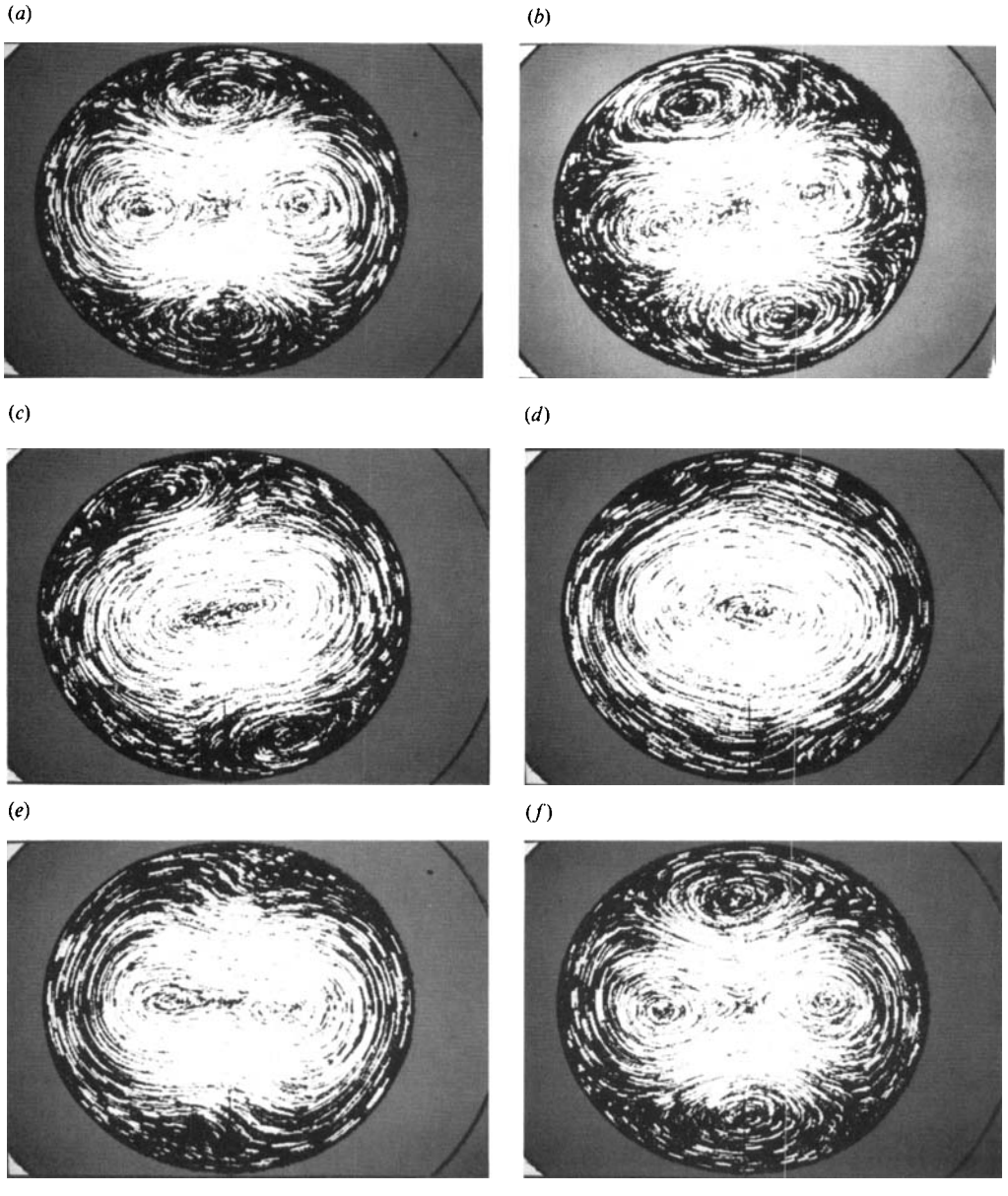

FIGURE 9. Streak photographs for FB topography at forcing phase angle (*a*) $-\frac{1}{2}\pi$, (*b*) $-\frac{1}{4}\pi$, (*c*) 0, (*d*) $\frac{1}{4}\pi$, (*e*) $\frac{1}{2}\pi$, (*f*) π, for $\delta = 0.02$ and $\tau = 20.0$ s ($\epsilon = 0.055$); $S = 0.052$. The hills are on the left and right; the valleys at the top and bottom. In this and all subsequent streak photographs the basic rotation is clockwise.

The reasons for the above behaviour are as follows. The WNL model fails for the FB cases because the parameters μ and ξ are such that $v_2 = \Psi_{2r}$ is fairly large (typically around -20) and $\sigma^2 = S^{\frac{2}{3}} \approx 0.2$ is not sufficiently small to render a convergence series in (9). The LO model is better because the extra (last) term in (15) effectively limits the growth of the zonal flow correction by adjusting the wavefield, yielding amplitudes which are essentially in agreement with experiments. Both models use a truncation to a single spatial wave (WNL is asymptotic in this respect, LO *ad hoc*). Near the resonance peaks the motion will be dominated by the linearly

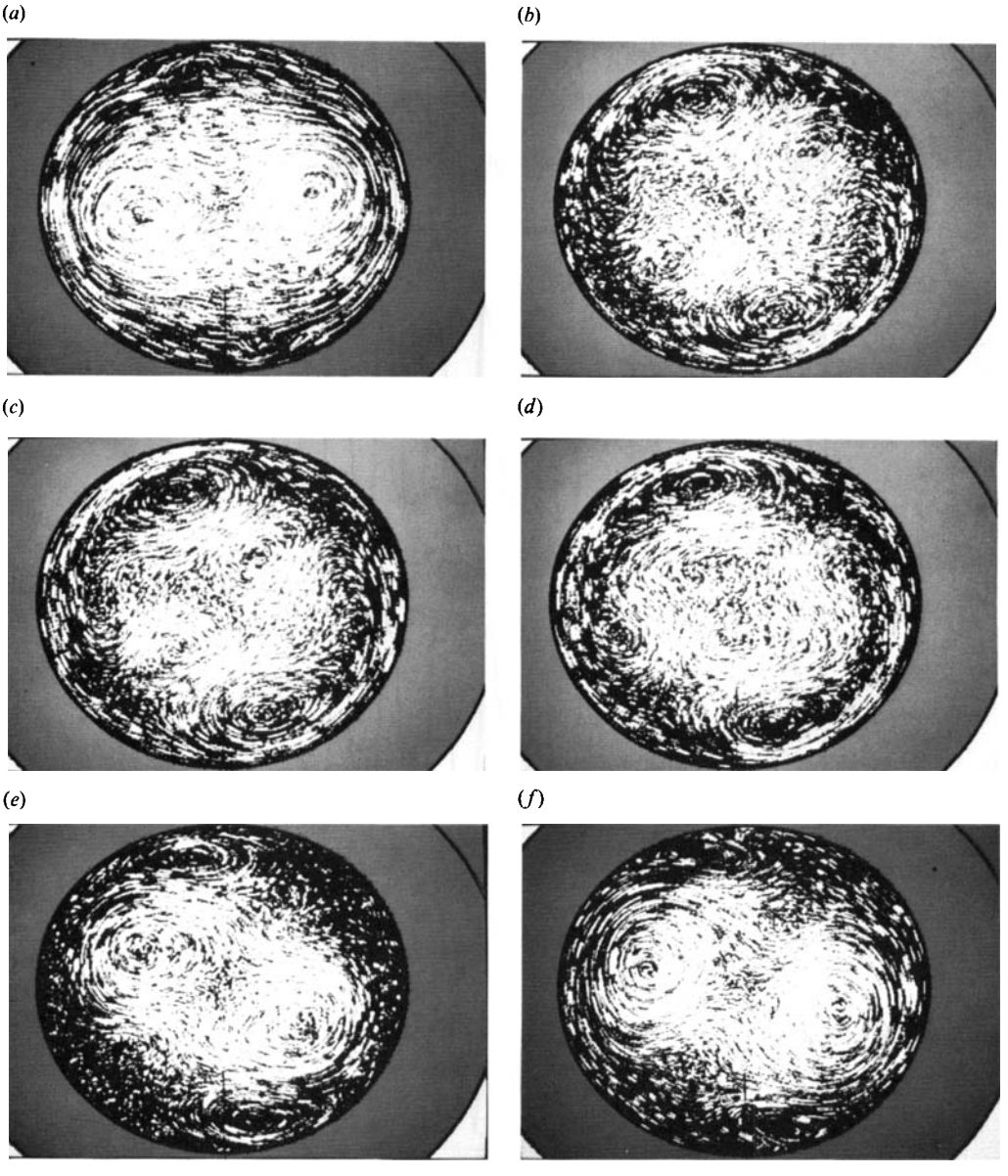

FIGURE 10. Streak photographs for FB topography at forcing phase angle (*a*) $-\frac{1}{2}\pi$, (*b*) $-\frac{1}{4}\pi$, (*c*) 0, (*d*) $\frac{1}{4}\pi$, (*e*) $\frac{1}{2}\pi$, (*f*) π, for $\delta = 0.02$ and $\tau = 50.0$ s ($\epsilon = 0.22$); $S = 0.32$. The hills are on the left and right; the valleys at the top and bottom.

resonant wave structure, and wave–wave self-interactions generate a large zonal flow. This zonal current advects the wave field (in both models), but for the substantial topography used here (with $h_B \approx 0.1$) it also generates waves itself (in the LO model only). If the wave amplitudes are not too great, the sideband wave interactions are numerically small compared with the zonal–fundamental interaction contained in the LO model. Off-resonant conditions which arise as τ, and hence S, are increased offer the possibility of stronger wave–wave interactions and the generation of spatial modes not included in the models.

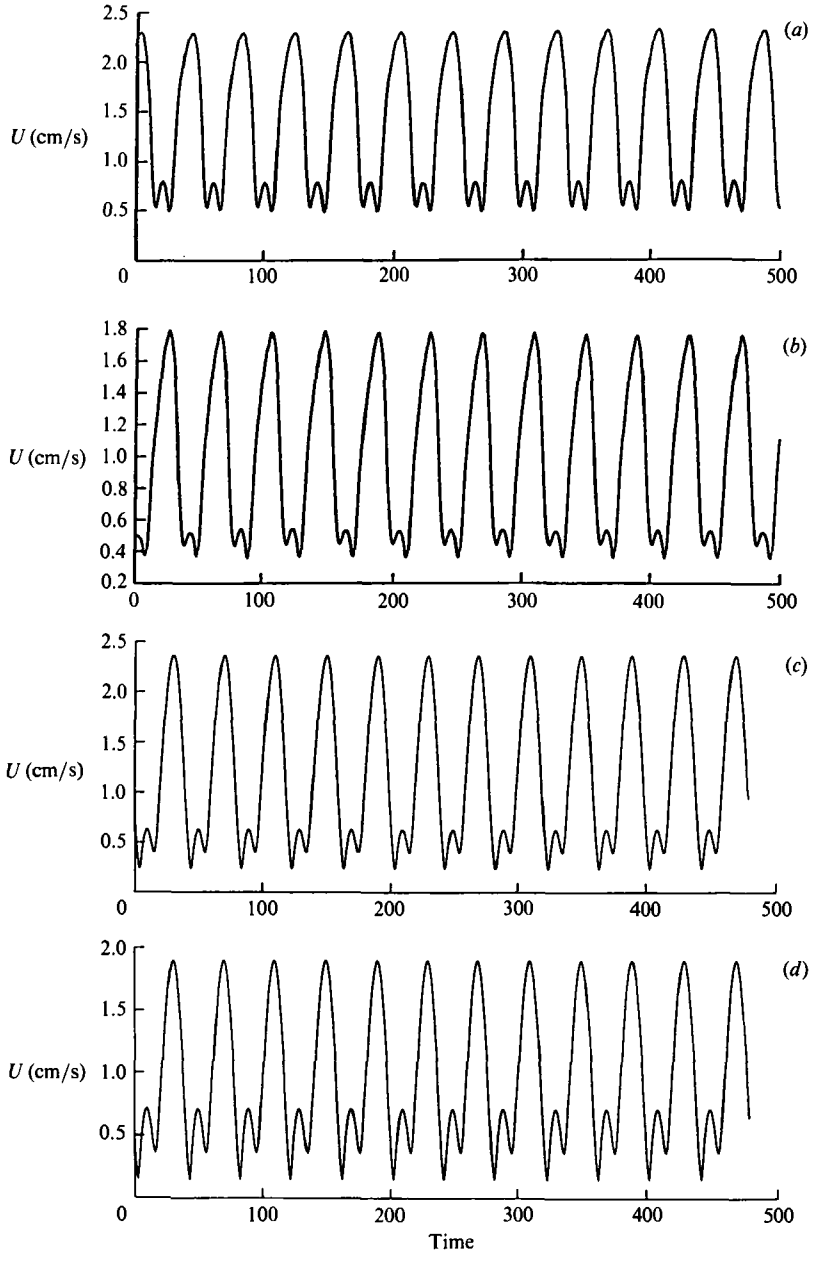

FIGURE 11. Time traces for experiments at $\mu^2/\xi^2 = 0.23$ and $\xi^{-3} = -0.30$ (a, b) and the WNL model at $\mu^2/\xi^2 = 0.23$ and $\xi^{-3} = -0.24$ (c, d).

Short-exposure time streak photographs support this latter idea. These were taken with an overhead CCD television camera viewing the upper free surface, which had been laced with aluminium powder flakes. The TV signal was fed into a MATROX image processing board attached to a personal computer. After thresholding to capture bright particles, successive frames coming in at a rate of 30 per s were OR'd together to produce instantaneous streamlines. Each streak 'exposure' time was small (typically 1 s) compared to the forcing period (typically 25 s or larger), so that the image gives an approximation to the instantaneous streamlines. Long-time

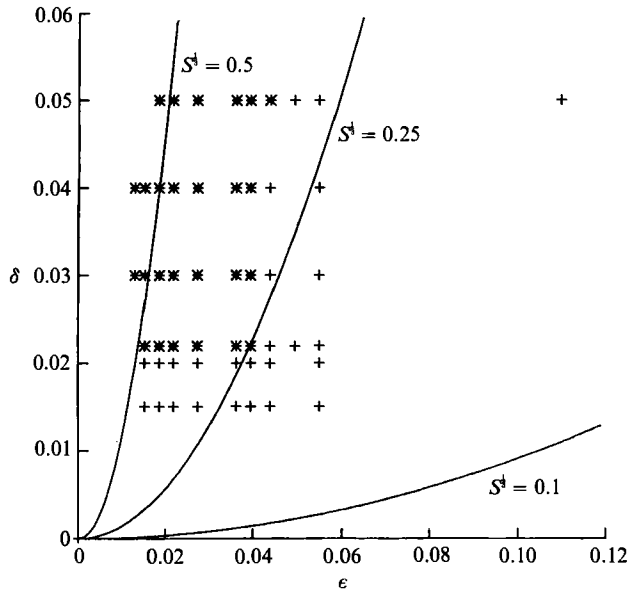

FIGURE 12. Regime diagram for US and $H_B = 0.10$. Chaotic time traces denoted by *, periodic ones by +.

trajectories may be obtained by a similar method with a greater exposure time, except that different surface floats must be used to prevent 'winking' and guarantee continuity of the trajectories. Such long-time measurements are described in §5. In all the following streak photographs the basic rotation Ω_0 is clockwise (which we define as cyclonic).

At $\tau = 20$ s (figure 9) the spatial structure is dominated by a pair of cyclonic vortices (over the valleys in figure 9*a*) and a pair of anticyclonic vortices (over the hills) which propagate first westward (counterclockwise, 9*a*, *b*) then eastward (clockwise, figure 9*c*–*e*), weakening as the modulation reaches a minimum during a forcing cycle (figure 9*e*). Note that the flow is dominated by $n = 2$ waves throughout. At $\tau = 50$ s, as the rotation rate of the tank begins to increase, the spatial pattern is again dominated by two anticyclonic vortices moving westward (counter-clockwise) over the hill, along with two smaller anticyclonic vortices in the valley (figure 10*a*). As in figure 9(*b*), when the tank reaches its greatest rotation rate, the two anticyclonic vortices begin to shrink in size and are pushed inwards leaving the two cyclonic vortices over the valleys (figure 10*b*, *c*). When the rotation rate begins to decrease the parts of the two cyclonic eddies that have extended over the top of the hills pinch-off and form four cyclonic vortices sitting at about $r = \frac{2}{3}$ (figure 10*d*). This pattern of four cyclonic vortices requires a term with $n = 4$ in the spatial spectral expansion, which is absent from the models. As the rotation rate further decreases, the two anticyclonic eddies move outwards and grow (figure 10*e*), until a pattern approaching the initial one is attained (figure 10*f*). This sequence shows that as S increases the models break down because the wavenumber-4 component of the motion becomes significant.

An attempt was made to find the multiple equilibrium solutions predicted by the WNL model. We have not determined the entire domain of multiple states because this is a hard task experimentally. The dual requirement of being within or near the predicted 'triangle' of multiple states, and simultaneously having parameters $S^{\frac{1}{3}}$, μ and ξ such that the weakly nonlinear expansion is reasonably accurate is difficult to

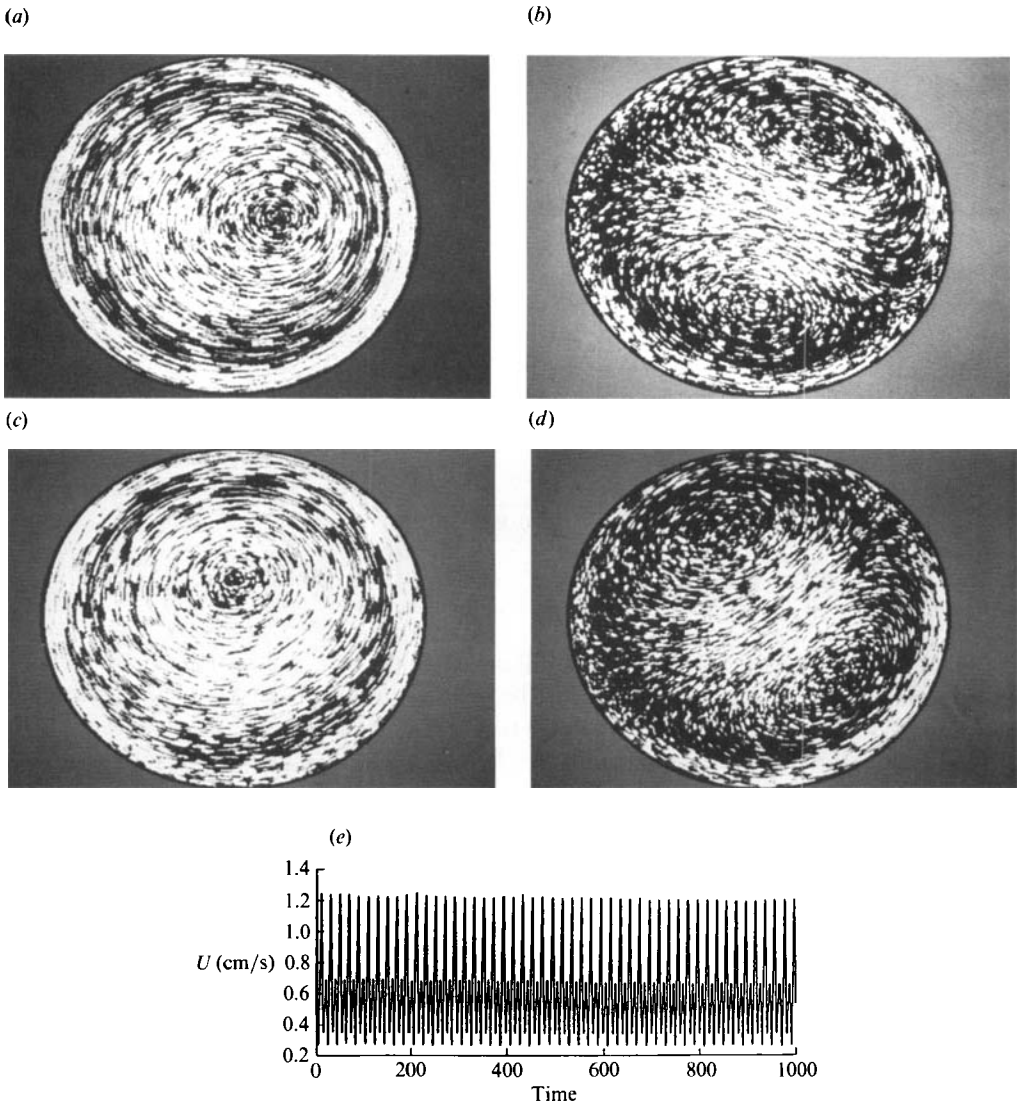

FIGURE 13. Streak photographs for US topography with $H_B = 0.1$ at forcing phase angle (*a*) 0, (*b*) $\frac{1}{2}\pi$, (c) π, and (*d*) $\frac{3}{2}\pi$. (*e*) Experimental time trace for $\delta = 0.05$ and $\tau = 20.0$ s ($\epsilon = 0.055$). The top of the hill is on the left-hand side of each picture, the valley on the right, and the basic rotation is clockwise.

satisfy over a range of conditions broad enough to pass from one state to the other in small well-controlled steps. Therefore we are constrained to sit in a narrow band of parameters and make many runs from different random initial conditions, looking for different end states. Figure 11 shows two experimental time series of flow speed for two different runs at the same external parameters $\mu^2/\xi^2 = 0.23$ and $\xi^{-3} = -0.30$, with US topography and $H_B = 0.05$. The WNL theory does reasonably well at predicting these waveforms for its two stable equilibria, as comparisons between figures 11 (*a*, *b*) and 11 (*c*, *d*) show. The multiple states were found experimentally in a slim band of ξ^{-3} values that are slightly more negative than the narrow range predicted by theory at this value of μ^2/ξ^2. Thus the model predictions are given for

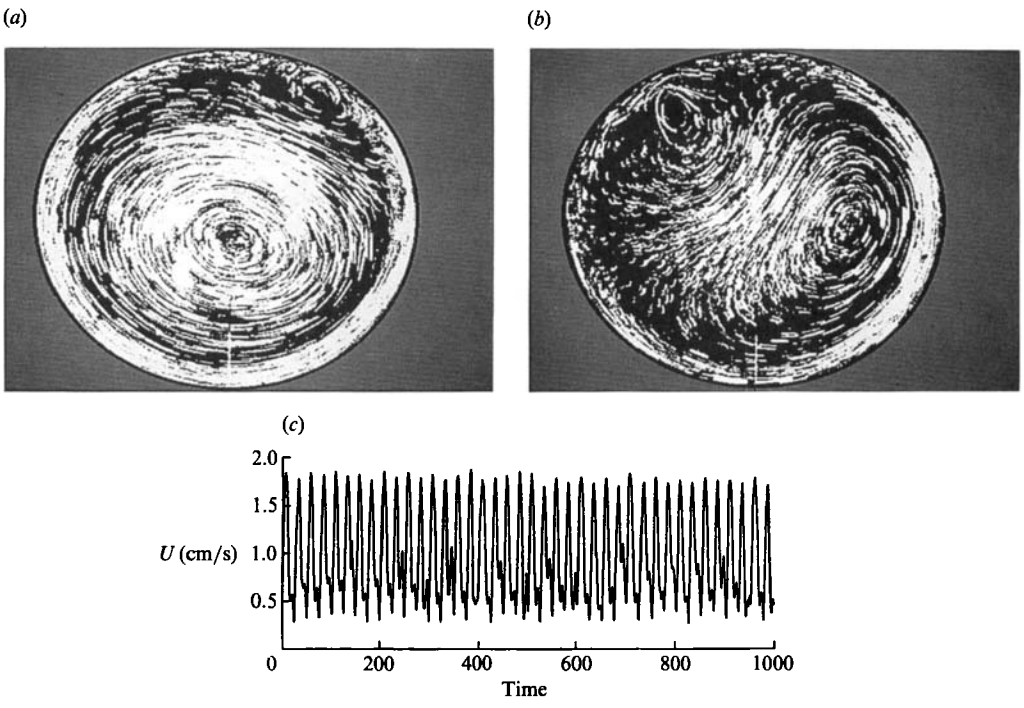

FIGURE 14. Streak photographs for US topography and $H_B = 0.1$ at forcing phase angle (*a*) $-\frac{1}{2}\pi$, and (*b*) $\frac{1}{2}\pi$. (*c*) Experimental time trace with $\delta = 0.050$ and $\tau = 22.2$ s ($\epsilon = 0.049$). The hill is on the left-hand side.

$\xi^{-3} = -0.24$, which is at the centre of a range for multiple equilibria that is approximately 0.02 units wide and centred on $\xi^{-3} = -0.24$, for the same value of $\mu^2/\xi^2 = 0.23$ that was used in the experiments.

4. Transition to chaotic flow

As δ increases and τ decreases the time series obtained from the thermistor probe eventually become non-periodic, as evidenced by a broadening of the spectral peaks in a Fourier transform of the data. Figure 12 shows the region of the (δ, ϵ)-parameter plane where Eulerian chaos occurs for the uniform slope topography of amplitude 1 cm, with other parameters fixed in accord with the data in table 1. Using simultaneous thermistor probe data and overhead streak photography it is possible to identify the flow structures responsible for the loss of periodicity in the motion. Figure 13 displays the flows associated with a periodic point on the regime diagram at moderately large δ. The oscillatory time series is generated by a wavenumber-1 disturbance that is superimposed on a strong zonal current in figures 13(*a*) and 13(*c*), which weakens in figure 13(*b*) and 13(*d*) where the topographically forced wavenumber 1 vortex dipole is more evident. At just slightly larger forcing period (smaller ϵ), the periodic signal becomes chaotic. Associated with this is a smaller scale eddy which is born in the sidewall boundary layer when the rotation rate is increasing (figure 14*a*), and which subsequently propagates westward and then out into the interior (figure 14*b*). During the following eastward (clockwise) sloshing phase the 'wall-eddy' can either dissipate in the interior or be reabsorbed into the sidewall boundary layer, depending on the values of the external parameters.

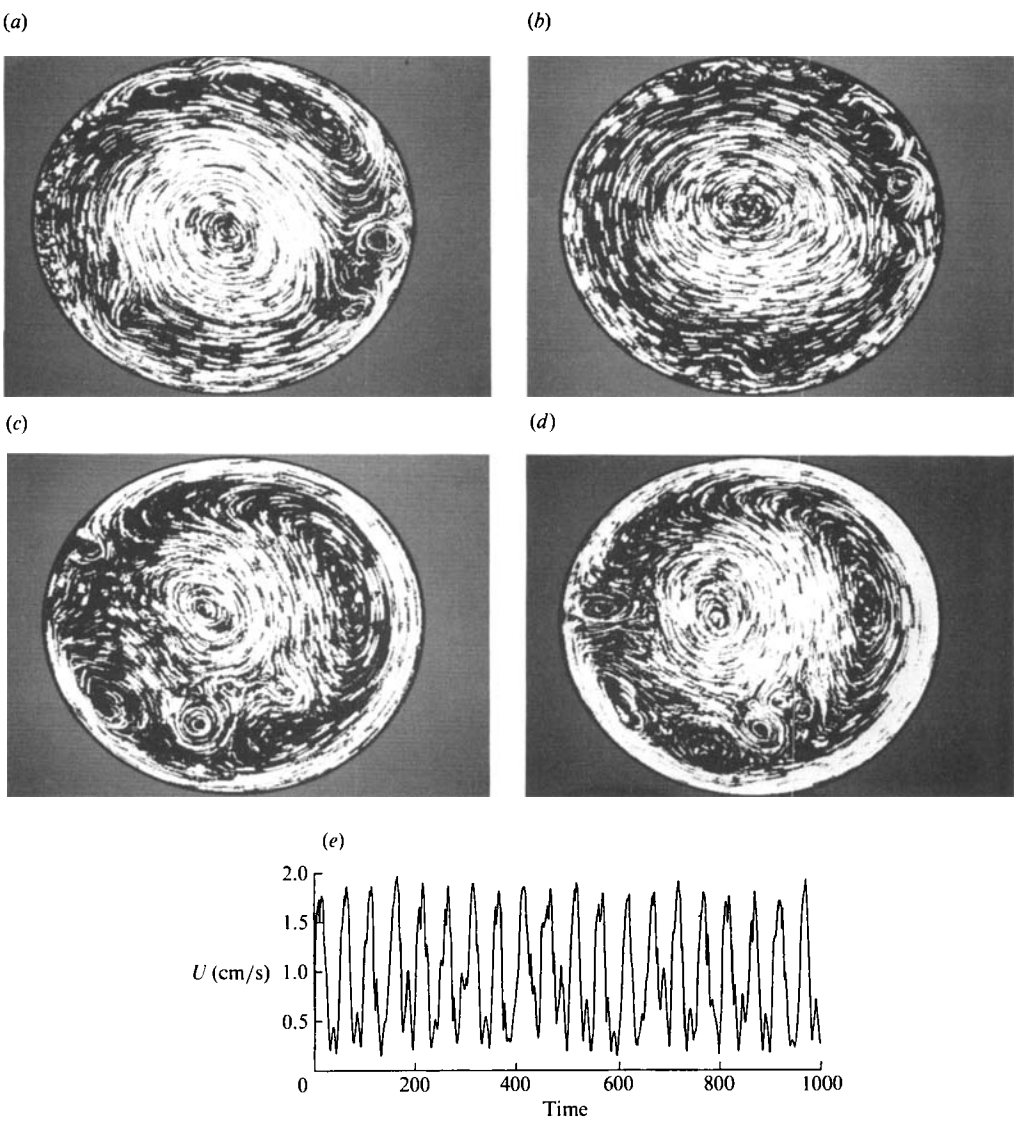

FIGURE 15. Streak photographs for US topography and $H_B = 0.1$ at forcing phase angle (*a*) $-\frac{1}{2}\pi$, (*b*) $-\frac{1}{4}\pi$, (*c*) π, and (*d*) $\frac{3}{2}\pi$. (*e*) Experimental time trace for $\delta = 0.050$ and $\tau = 50.0$ s ($\epsilon = 0.040$). The hill is on the left-hand side and the basic rotation is clockwise.

Further into the chaotic regime a series of wall eddies can be born and mixed into the interior, leading to a more aperiodic time series (figure 15). A similar transition process occurs at lower δ, where the boundary-layer vortex generation and shedding appears to cutoff sharply as δ is decreased. This is illustrated in figure 16 which again shows the small-scale eddy characteristic of the chaotic regime for $\delta = 0.022$, with smooth boundary layers for $\delta = 0.020$.

The situation for the FB topography is essentially the same. Figure 17 gives the regime diagram. Chaos occurs at low Rossby number ϵ based on frequency, which corresponds to a large topographic forcing parameter S (see table 1), and at large flow Rossby number δ. The bounding curve is nearly at constant S. This may or may not be dynamically significant because other parameters (β, η, Q, E_L) are varying along

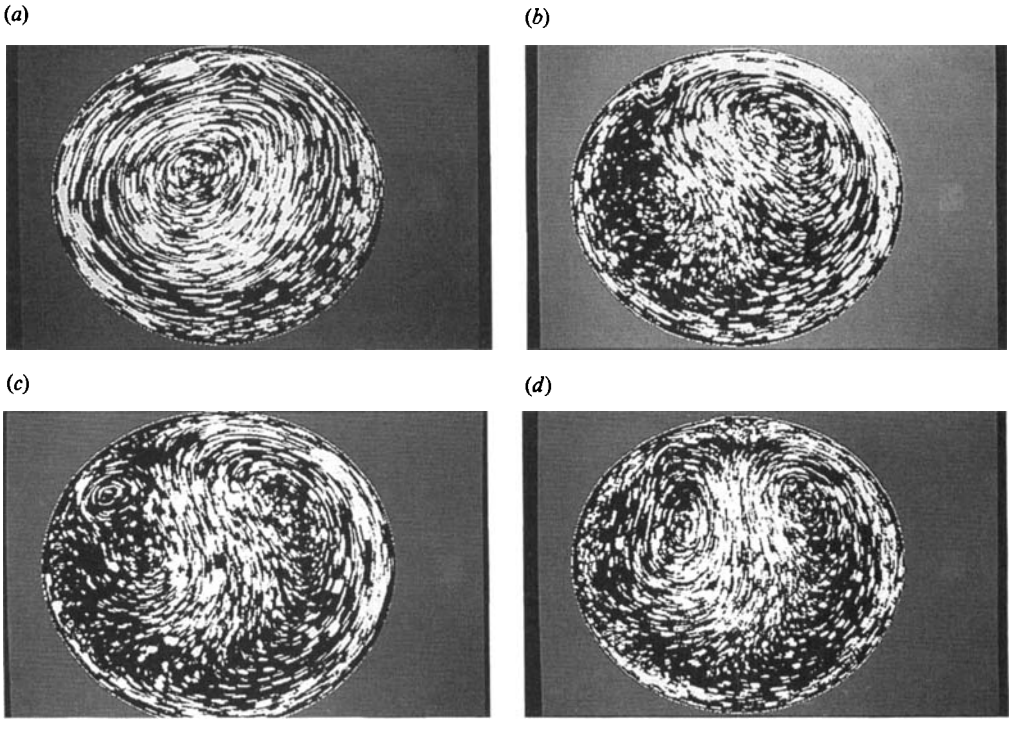

FIGURE 16. Streak photographs for US topography and $H_B = 0.1$ at forcing phase angle (*a*) $\frac{1}{4}\pi$, (*b*) $\frac{1}{2}\pi$, and (*c*) π, for $\delta = 0.022$, and (*d*) π for $\delta = 0.020$ with $\tau = 27.8$ ($\epsilon = 0.040$). The hill is on the left-hand side of each picture.

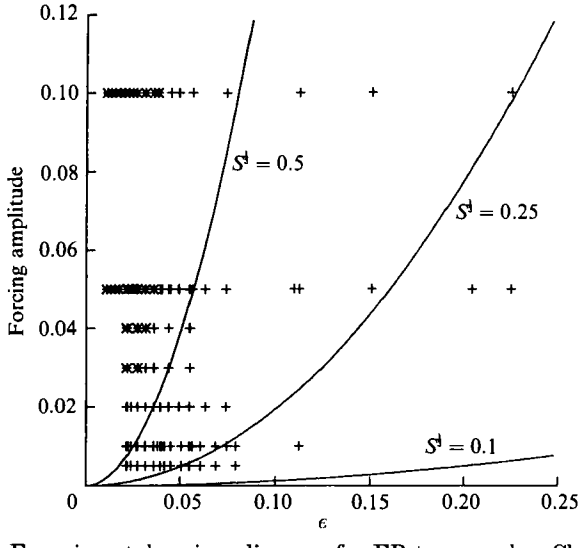

FIGURE 17. Experimental regime diagram for FB topography. Chaotic time traces denoted by *, periodic ones by +.

isolines of S. Typically, as the rotation rate of the tank begins to increase from its smallest value, wall eddies are formed in the boundary layer on the eastern sides of the valleys, near the larger interior cyclonic vortices which were present at similar forcing phases in the periodic cases. The wall eddies propagate westward (figure 18*b*),

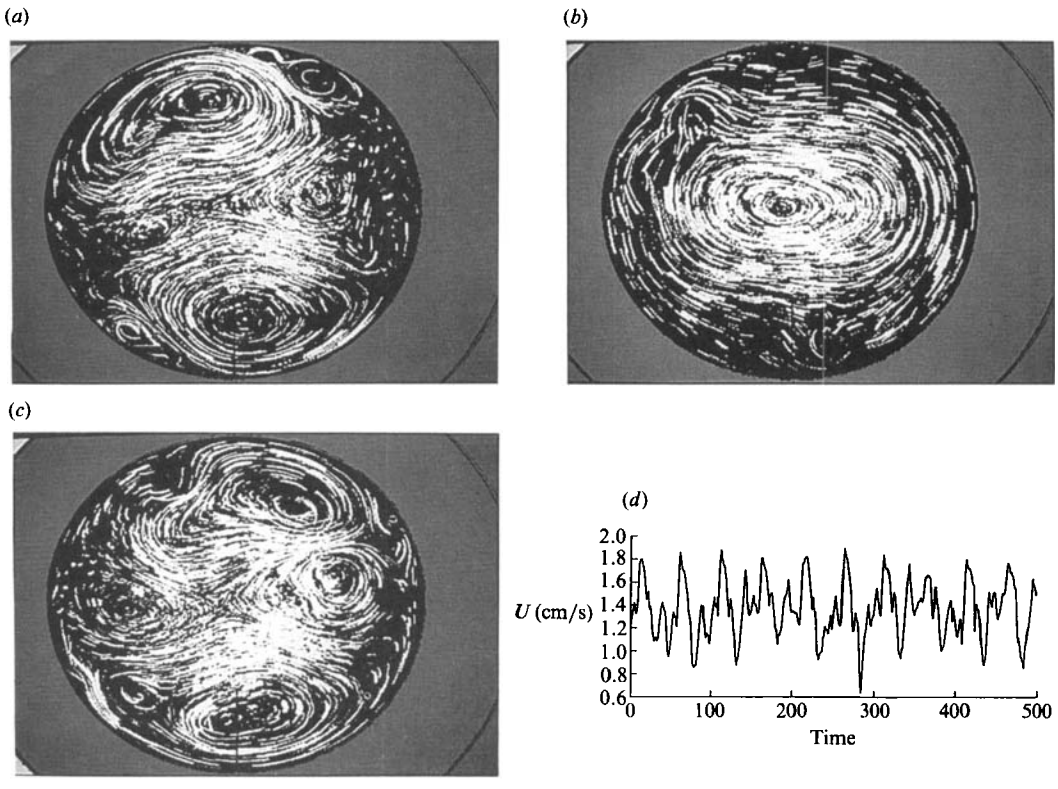

FIGURE 18. Streak photographs for FB topography at forcing phase angle (*a*) $-\frac{1}{2}\pi$, (*b*) 0, (*c*) π and (*d*) experimental time trace with $\delta = 0.05$ and $\tau = 50.0$ s ($\epsilon = 0.022$). The hills are on the left and right; the valleys on the top and bottom.

break loose from the boundary and again cause rather violent perturbations to the interior motions (figure 18*c*).

5. Parcel trajectories

In this section we compare model Poincaré sections with experimental ones. The former are generated by first solving (14)–(16) numerically. After a statistically stationary solution is obtained, the particle path equations are integrated simultaneously for several test particles. The path equations form a $1\frac{1}{2}$-degree-of-freedom nonlinear Hamiltonian system given by

$$\frac{\mathrm{d}r}{\mathrm{d}t} = u = n[Y(t)\cos(n\theta) - X(t)\sin(n\theta)]\,J_n(\alpha_{nm}\,r), \tag{20}$$

$$\frac{\mathrm{d}\theta}{\mathrm{d}t} = \frac{v}{r} = -\frac{\delta}{2\epsilon}\sin(t) + [X(t)\cos(n\theta) + Y(t)\sin(n\theta)]\frac{\alpha_{nm}\,J_n(\alpha_{nm}\,r)}{r} + Z(t)\frac{J_n^2(\alpha_{nm}\,r)}{r^2}, \tag{21}$$

where the stream function $\Psi(r, \theta, t)$ serves as the Hamiltonian.

Experimental trajectories are obtained by OR'ing together many forcing cycles of successive overhead video pictures of surface floats. Two float types were used: small 0.25 cm diameter vinyl discs that adhere to the surface via tension, and soggy cork discs whose topsides remain at the surface but whose bulk is underwater like an

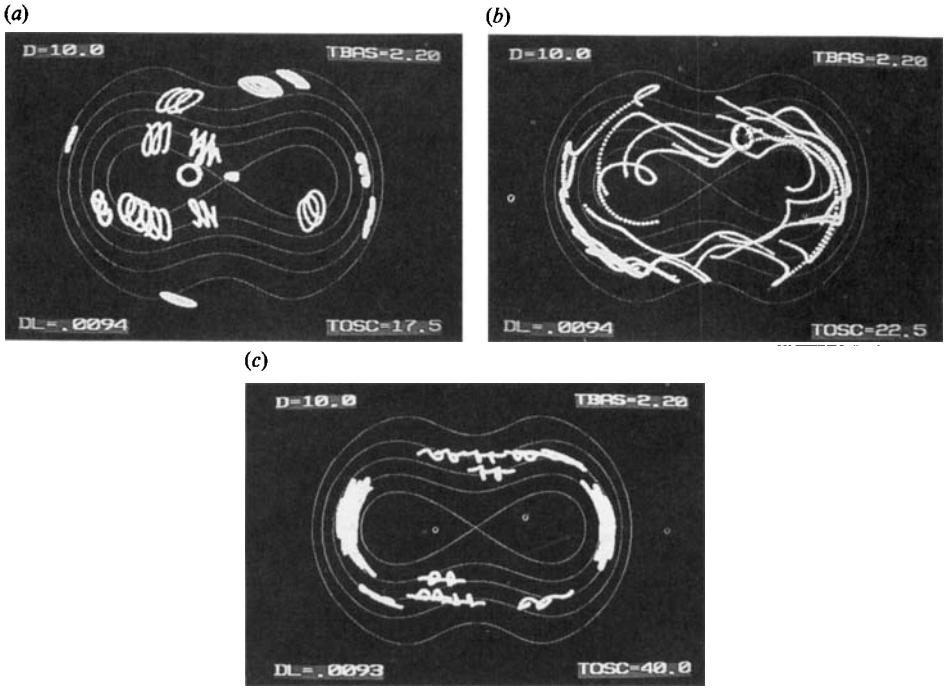

FIGURE 19. Trajectories for FB topography at $\delta = 0.009$ and (*a*) $\tau = 17.5$ s, (*b*) $\tau = 22.2$ s, and (*c*) $\tau = 40.0$ s. The time of exposure is different for each. Thin lines show static thickness contours (hills at left and right). The basic rotation is clockwise.

iceberg. Equivalent data were obtained for each, suggesting an absence of surface-tension effects on the floats. Direct Poincaré sections were obtained by looking at a few floats over hundreds of forcing cycles. At a fixed phase of each forcing cycle a single video frame was taken and OR'd with a buffer containing all previous strobed frames. The final image then represents the (r, θ)-positions of vertical fluid columns during successive phases $\alpha + 2k\pi$ $(k = 0, 1, 2, \ldots)$ of the forcing.

Figure 19 shows a typical example of the experimental parcel trajectories, which can be periodic or chaotic. In these examples the Eulerian flow is always periodic, but near the flow resonance the trajectories are chaotic (figure 19*b*). The orbits drift in the retrograde (counter-clockwise) sense, as one would expect from the presence of the substantial negative mean zonal current predicted by the theories. The drifts tend to follow isobaths. If relative vorticity were much smaller than potential vorticity, this would be expected from conservatism of $2\Omega_0/(D+h-h_b)$ following fluid columns when friction is small. Here the isobath tracking is only approximate as relative vorticities are not negligible.

Experimental and theoretical Poincaré sections are shown in figure 20. The qualitative interpretation of the sections does not depend on the triggering phase angle α. Different values only serve to rotate and deform slightly the major features (e.g. compare figures 10*a* and 20*c*), as the maps are differentially equivalent. At parameter values where the LO model gives a good description of the flow, the associated theoretical Poincaré sections compare well with the data. Figure 21 addresses a case where the Eulerian flow is a very stable limit cycle (see figure 17). The chaotic and periodic parts of the Poincaré sections are well predicted by (14)–(21). The chaotic behaviour has expanded from the hyperbolic fixed points in

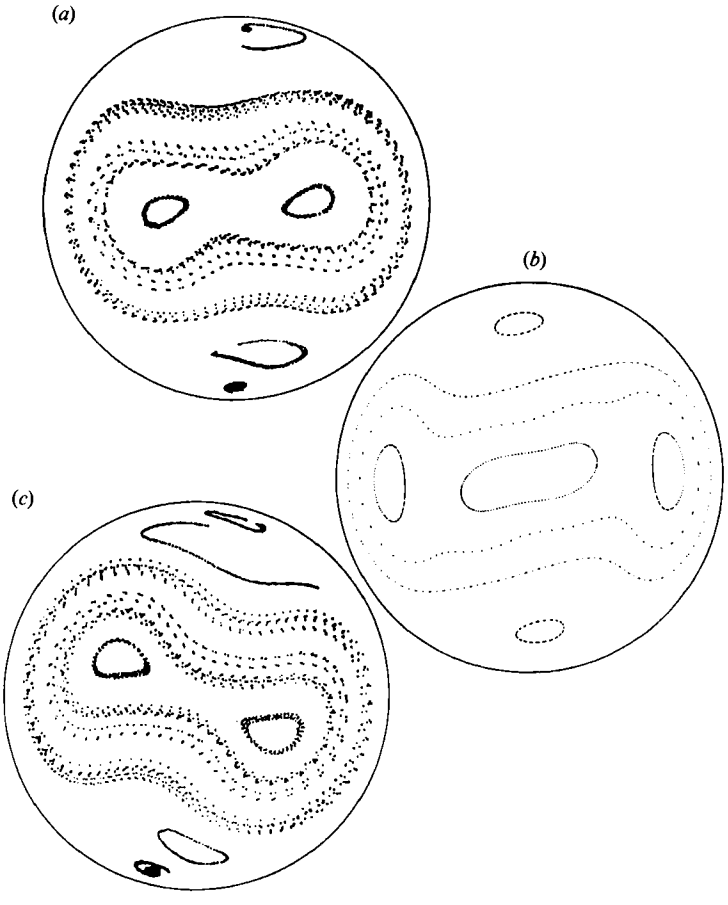

FIGURE 20. Poincaré sections with the FB topography for $\delta = 0.010$ and $\tau = 17.5$ s ($\epsilon = 0.063$) at forcing phase angles: (*a*) 0 (experimental), (*b*) 0 (LO model), and (*c*) π (experimental).

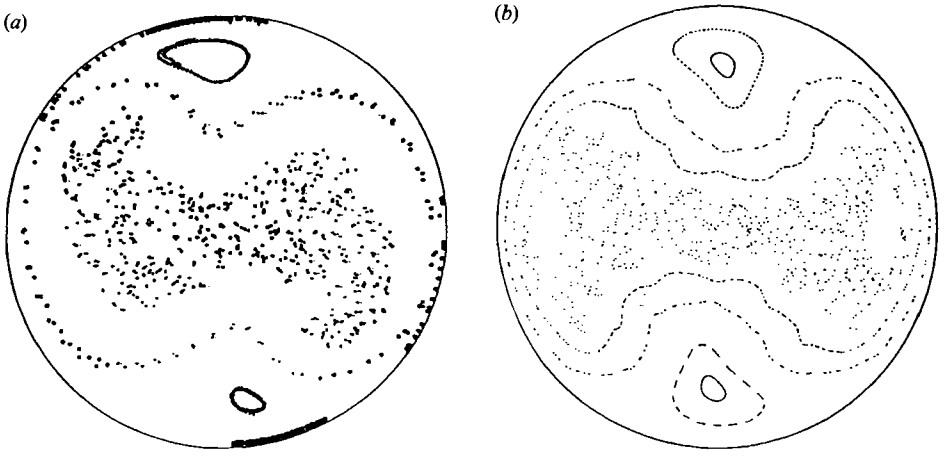

FIGURE 21. Poincaré sections with the FB topography for $\delta = 0.005$ and $\tau = 21.7$ s ($\epsilon = 0.051$) at forcing phase angle zero: (*a*) experimental, (*b*) LO model.

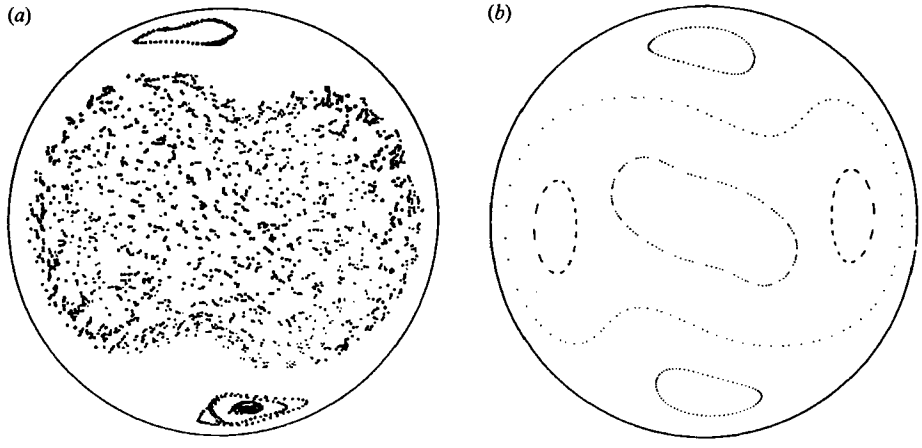

FIGURE 22. Poincaré sections with the FB topography for $\delta = 0.010$ and $\tau = 30.3$ s ($\epsilon = 0.036$) at forcing phase angle zero: (*a*) experimental, (*b*) LO model.

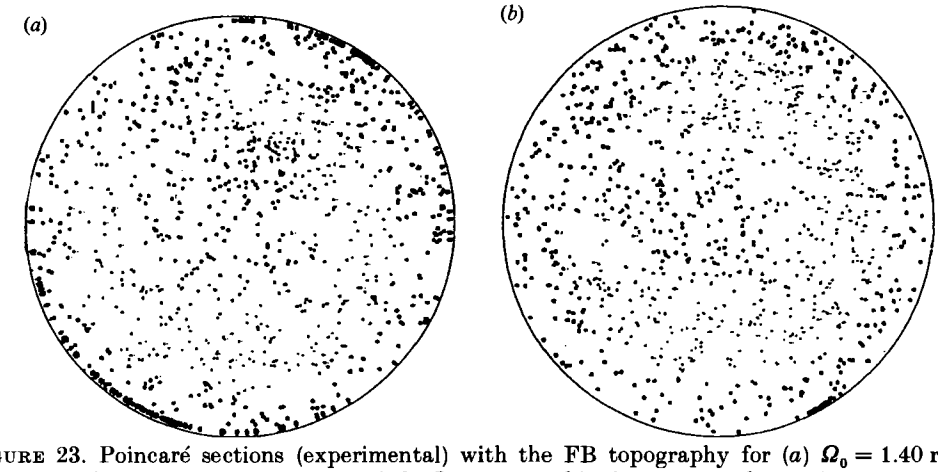

FIGURE 23. Poincaré sections (experimental) with the FB topography for (*a*) $\Omega_0 = 1.40$ rad/s, $\delta = 0.10$ and $\tau = 58.8$ s ($\epsilon = 0.038$), and (*b*) $\Omega_0 = 2.85$ rad/s, $\delta = 0.050$ and $\tau = 50.0$ s ($\epsilon = 0.022$).

the interior over the hills to fill a substantial area bounded by close KAM curves where periodic orbits are found. The KAM curves isolate the chaotic trajectories in the interior from those with a more regular behaviour out over the valleys. Mixing across these boundaries is not observed. In the outer valleys the particle paths are mostly periodic, with small areas of chaos near the hyperbolic fixed points that lie on the wall.

The next example (figure 22) is for another stable periodic Eulerian flow. Here, however, the LO model does not work as well as in figure 21 because the parameter point lies between the resonances where multiple spatial modes are found (see figure 7). δ has increased and the area of Lagrangian chaos has expanded, but the theory, now based on an incorrect Eulerian velocity field, is almost everywhere regular. When the experimental parameters are finally pushed into the region of Eulerian chaos (shown in figure 17), the wall eddies cause a mixing of fluid parcels initially near the outer wall into the interior. Then the last stable islands near the rim in figures 22 and 21 are destroyed, yielding completely chaotic sections as illustrated in figure 23. Here the LO model also predicts area-covering chaos, but this is only due

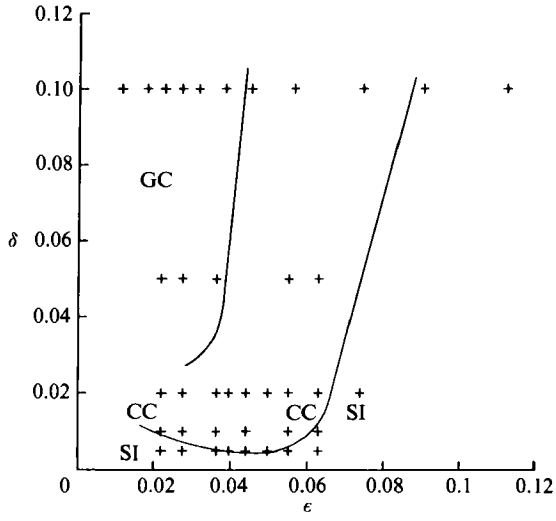

FIGURE 24. Regime diagram for experimental Poincaré sections with FB topography. SI, stable islands; CC, confined chaos; GC, global chaos.

to the overly large amplitudes of the periodic Eulerian flow that it gives for these highly nonlinear parameter settings where both δ and $S^{\frac{1}{3}}$ are large.

The Poincaré section data are summarized in figure 24. The states SI refer to situations where less than 10% of the tank surface is occupied by chaotic regions at phase angle zero, the rest is filled with stable islands (i.e. closed KAM curves signifying quasi-periodic motion). Globally chaotic states (GC) have less than about 10% of the tank occupied by quasi-periodic particle paths. Confined chaotic states (CC) lie in between these two extremes. This rather rough attempt at a qualitative characterization serves to illustrate the points that (i) periodic flows can be accompanied by localized chaotic parcel trajectories, and (ii) that globally chaotic fluid paths are observed precisely for those parameter values where the Eulerian field itself is chaotic due to the presence of wall eddies.

6. Conclusions

We have reported laboratory experimental observations on periodically forced flow over topography in a rotating cylinder. The results permit some comparisons with weakly nonlinear and low-order models in this situation, and provide interesting data in strongly forced regimes that we hope will stimulate further theoretical and numerical studies. The weakly nonlinear model captures the main qualitative features of the observed flow. It predicts the observed shifting of the peak response or resonance from the linear value to supercritical values of the forcing period for topography with wavenumber $n = 1$, and to subcritical values for topography with wavenumber $n = 2$. It forecasts a retrograde time-mean zonal current produced by wave self-interactions, and predicts the presence of multiple equilibria. Both of these signatures of the WNL model were observed experimentally. This model gives useful quantitative predictions when the expansion parameter S is small enough that the predicted retrograde flow (of order $S^{\frac{2}{3}} \times \Psi_{2r}(Q, \beta, \eta, S, r)$) is much smaller than the basic sloshing motion (of order δ/ϵ). If the parameters are pushed beyond what might

normally be expected for validity of a weakly nonlinear theory, the retrograde mean motion eventually swamps the rest of the solution. Because there is no interaction between this large retrograde flow and the topography, the weakly nonlinear theory then fails.

A low-order model which includes the interaction of the wave-generated zonal currents with the topography was introduced and was shown to work reasonably well when the spatial structures included in the truncation are dominant in the observed field. This is the case when the forcing δ and frequency Rossby number ϵ are such that (i) the Eulerian flow is periodic, and (ii) the system is near the primary nonlinear resonance at small to modest δ and $S^{\frac{1}{3}}$. Interesting circumstances have been studied theoretically where more than one spatial mode can be simultaneously resonant (Jones 1989). However, such cases do not commonly occur with the single-mode or uniform-slope topographies studied here.

Chaotic Eulerian flows are found in the experiments as the frequency Rossby number ϵ is decreased and the forcing amplitude δ is increased. They are associated with wall eddies that arise in the sidewall boundary layer at one phase during the forcing cycle and then propagate into the interior in an erratic manner. The transition between periodic and chaotic flows is quite sharp and with our current apparatus we have been unable to isolate a purely periodic or quasi-periodic wall-eddy flow. The two theories discussed here do not reproduce this phenomenon as they have limited spatial representation and no rigid outer wall. The dynamical mechanism for the generation of the wall eddies is not obvious. Experiments with a flat bottom show no tendency for such phenomena (i.e. $S^{\frac{1}{3}}$ has to be fairly big for it to occur). This suggests that pressure gradients along the wall due to interior–boundary interactions in the presence of interior topography may be important. Such pressure gradients can lead to boundary-layer separation. The regime diagrams presented here may be useful for theoretical or numerical modelling of this process.

Finally, experimental Poincaré sections show complex folding and stretching of fluid parcels for periodic Eulerian flows. Such situations are successfully modelled by integrations of the trajectory equations using the predicted (and periodic) motion fields from the low-order theory, provided the parameters are set to values for which the low-order model itself is reasonably accurate. Complete mixing over the entire experiment appears to occur only when the Eulerian flow becomes chaotic with wall eddies that carry boundary fluid into the centre of the tank.

The authors thank the National Science Foundation for support of this research under grant OCE-8918589 to the University of Colorado.

REFERENCES

ALLEN, J. S., SAMELSON, R. M. & NEWBERGER, P. A. 1991 Chaos in a model of forced quasi-geostrophic flow over topography: an application of Melnikov's method. *J. Fluid Mech.* **226**, 511–547.

CHARNEY, J. G. & DEVORE, J. G. 1979 Multiple flow equilibria in the atmosphere and blocking. *J. Atmos. Sci.* **36**, 1205–1216.

DENBO, D. W. & ALLEN, J. S. 1983 Mean flow generation on a continental margin by periodic wind forcing. *J. Phys. Oceanogr.* **13**, 78–92.

HAIDVOGEL, D. B. & BRINK, K. H. 1986 Mean currents driven by topographic drag over the continental shelf and slope. *J. Phys. Oceanogr.* **16**, 2159–2171.

HART, J. E. 1972 A laboratory study of baroclinic instability. *Geophys. Fluid Dyn.* **3**, 181–209.

HART, J. E. 1979 Barotropic quasi-geostrophic flow over anisotropic mountains: multi-equilibria and bifurcations. *J. Atmos. Sci.* **36**, 1736–1746.

HART, J. E. 1990 On oscillatory flow over topography in a rotating fluid. *J. Fluid Mech.* **214**, 437–554.

JONES, S. W. 1989 Multiple resonant topographic waves in barotropic flow. *GFD Summer School Notes, Woods Hole Tech. Rep.* WHOI-89-54, pp. 392–407.

PEDLOSKY, J. 1987 *Geophysical Fluid Dynamics.* Springer, 624 pp.

PRATTE, J. M. 1990 A study of oscillatory flows over topography in a rotating system. Ph.D. thesis, University of Colorado, 160 pp.

SAMELSON, R. M. & ALLEN, J. S. 1987 Quasi-geostrophic topographically generated mean flow over a continental margin. *J. Phys. Oceanogr.* **17**, 2043–2064.